Available online at www.sciencedirect.com

ScienceDirect

IFAC PapersOnline CONFERENCE PAPER ARCHIVE

IFAC PapersOnLine 55-31 (2022) 178–183

Chemical plume tracking using an AUV with UKF based extremum seeking ⋆

Tim Benedikt von See * **Thomas Meurer** ** **Jens Greinert** *

* *GEOMAR Helmholtz-Center for Ocean Research Kiel (e-mail: {tsee, jgreinert}@geomar.de*

** *Chair of Automation and Control, Faculty of Engineering, Kiel University, (e-mail: tm@tf.uni-kiel.de)*

Abstract: Hydrothermal vent areas are unique ecosystems with high productivity and high biodiversity that are subject to ongoing research. Hydrothermal vents form in areas with increased magmatic activity where superheated, mineral rich water leaks from the seafloor. Due to the rapid cooling of the water the metal sulfides precipitate and form a black or white plume that can be sensed several hundred meters away from the vent source. Finding and reliably following such plumes with autonomous underwater vehicles (AUVs) is a challenging task since the plume does not have a smooth concentration gradient but lots of local patches due to the turbulent particle flow. This paper presents an algorithm that combines biology inspired chemotaxis with Unscented Kalman filter (UKF) based extremum seeking control (ESC). The effectiveness is demonstrated by a simulation of a physics-based AUV model in a turbulent 3D Plume model.

Keywords: AUV, Kalman filter, extremum seeking control, hydrothermal vents

1. INTRODUCTION

Autonomous underwater vehicles (AUVs) have become a standard gear in ocean science for conducting surveys. While the main use of AUVs is still to do surveys in the classical lawn mover patterns the interest in intelligent navigation and situational awareness for AUVs to find or to track features of scientific interest is growing fast. One actively studied application is to find hydrothermal vents. These are structures that form in areas with increased magmatic activity and particularly when two tectonic plates are diverging as on the mid ocean ridges. The water beneath the seafloor is heated up which leads to dissolving of minerals in rocks. When this superheated water leaks from the seafloor it is rapidly cooled down by the surrounding water of around 4 °C. The metal sulfides precipitate forming a black or white plume of very fine particles. Due to lower density the water rises (buoyant phase) until it reaches a water layer with the same density where the plume spreads predominantly horizontally in the direction of the currents (none-buoyant phase). The plume can be detected by three characteristics as described in Baker (2014): First, very close to the vent there is a large temperature gradient of the water. Second, up to a few hundred meters away from the source the redox value of the water is different from its surrounding water and third, a change in the turbidity of the water can in some cases be measured even several kilometers away from the source.

The first papers that dealt with AUV based plume detection focused on detecting the plume while driving classical lawn mover patterns, e.g. Jakuba and Yoerger (2008); Ferri et al. (2010). In Jakuba and Yoerger (2008) the authors apply occupancy grid mapping with a newly designed update rule. The result is a map that indicates coverage of the region as well as possible hydrothermal vent locations. The authors of Ferri et al. (2010) propose to drive spiral patterns with increasing depth when a trigger condition is met along the pre-planned lawn mover pattern. As trigger they use a low redox potential as is it a distinct feature for young plumes. The trigger threshold is adapted during the mission based on the percentage of triggered spirals with respect to the expected ones and the percentage of the covered track lines of the pre-planned path. Another approach is to follow the plume up-current to find the hydrothermal vent. Most papers in this direction are inspired by the chemo-tactic behavior of animals such as male moths which are able to follow a pheromone plume of female moths as, e.g., observed in Elkinton et al. (1987). The authors of Li et al. (2006) try to mimic this behavior as close as possible with a behavior switching diagram. Real world test are performed with an AUV that traces a plume of Rhodamine dye in the horizontal plane. In Tian et al. (2014) the authors propose a moth inspired behavior based strategy for the none-buoyant and the buoyant phase of the plume. The four behaviors 'track-in', 'track-out', 're-acquire plume' and 'declare source' are designed where 'track-in' and 'track-out' result in the up-current zigzag trajectory in the none-buoyant phase and in a three dimensional spiral in the buoyant phase. The AUV switches from the none-buoyant to the buoyant search mode when a vertical current or a significant reduction-oxidation potential is detected. The authors of Wang et al. (2020) propose a chemical plume tracking strategy with a horizontal and a vertical search mode. In the horizontal

⋆ The first author is funded through the Helmholtz School for Marine Data Science (MarDATA), Grant No. HIDSS-0005. Parts of the work of the first author have been performed at the Kiel University at the Chair of Automation and Control.

10.1016/j.ifacol.2022.10.428

mode the AUV navigates up-current or drives in circles if the contact to the plume is lost, in the vertical mode the AUV drives a three dimensional spiral. The search mode is switched when the time in which no chemical is detected exceeds a threshold. A simulation based on real plume data is presented. In Vergassola et al. (2007) an algorithm called 'infotaxis' is proposed which locally maximizes the expected rate of information gain. It is designed for situations in which the desired tracer can only be sensed intermittently. The efficiency is demonstrated by simulations. A method for chemical plume tracking that is not bio-inspired is presented in Hu et al. (2019). Here the two dimensional plume tracking problem is modeled as partially observable Markov decision process and solved via long short-term memory-based Reinforcement learning with dynamic programming.

The method that is proposed in this paper is a combination of following the plume up-current and extremum seeking control (ESC) in the vertical and cross current direction based on von See et al. (2021). Even though the current direction is used this approach does not rely on expensive current measurement units such as an acoustic Doppler current profiler (ADCP). Instead a single drift maneuver at the start to estimate the current direction is sufficient. A pre-condition for such a drift maneuver is that the AUV has hovering capability. In environments with fast changing current angles this procedure could be performed in fixed intervals. Another contribution is that by integrating the vertical axis in the ESC this approach does not rely on measurement of vertical currents or reduction-oxidation potentials to detect the plume bending.

The paper is structured as follows. Section 2 presents the Unscented Kalman Filter (UKF) based ESC and the adaption to the plume tracking problem. In Section 3 the AUV model, simulation framework and simulation data are presented followed by the simulation results in Section 4. The paper is concluded in Section 5.

2. PLUME TRACKING ALGORITHM

2.1 UKF based extremum seeking control

The ESC loop that is used here is based on Lutz et al. (2019) and is shown in Fig. 1. The nonlinear time variant system $\Sigma(t, \boldsymbol{u}) : \mathbb{R}_0^+ \times \mathbb{R}^m \rightarrow \mathbb{R}^p$ with uncertain dynamics with the system input vector $\boldsymbol{u}(t) \in \mathbb{R}^m$ and the measurement vector $\boldsymbol{y}(t) \in \mathbb{R}^p$ together with the cost function $J_c(\boldsymbol{y})$ and the penalty function $p(\boldsymbol{u}, \boldsymbol{y})$ build the input/output map at the top.

Assumption 1. The system is either asymptotically stable or stabilized by an underlying control loop.

Assumption 2. The system dynamics are fast so that the influence of the system dynamics on the cost function can be neglected.

The ESC algorithm is composed of an UKF as gradient estimator and an optimization scheme. The sum of the cost function $J_c(\boldsymbol{y})$ and the penalty function $p(\boldsymbol{u}, \boldsymbol{y})$ yields the the cost function $\bar{J}_c(\boldsymbol{u}, \boldsymbol{y})$. By *Assumption 2* $\bar{J}_c(\boldsymbol{u}, \boldsymbol{y}) = J(\boldsymbol{u})$, at least on a small time scale, which is necessary for ESC to be applicable. The cost function $J(\boldsymbol{u})$ is given as input to the UKF that is used to estimate the gradient of the cost function $(\nabla_{\boldsymbol{u}} J)_{\text{est}}$ which is processed

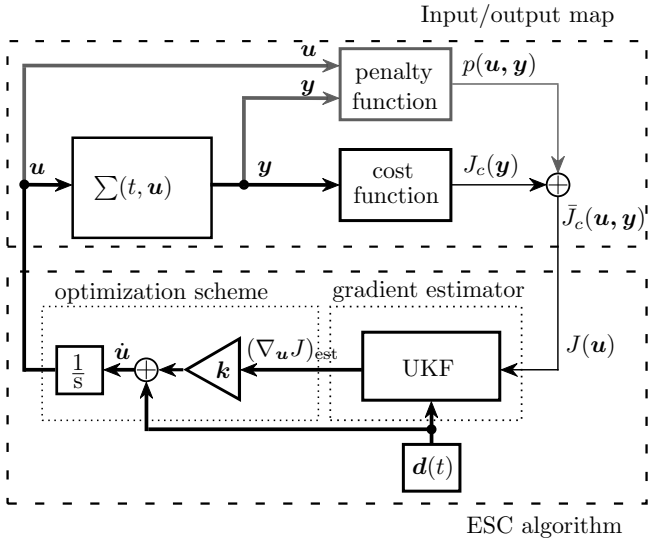

Fig. 1. ESC loop for an asymptotically stable system $\Sigma(t, \boldsymbol{u})$ with input $\boldsymbol{u}$, output $\boldsymbol{y}$, cost function $\bar{J}(\boldsymbol{u}, \boldsymbol{y}) = J(\boldsymbol{u})$ and penalty function in gray, proposed in Lutz et al. (2019).

in the optimization scheme to drive the system $\Sigma(t, \boldsymbol{u})$ to its maximum or minimum for the control gain $\boldsymbol{k}$ with $k_i > 0$ or $k_i < 0 \; \forall i \in 1, ..., m$, respectively.

For the sake of self-containedness and to motivate the application, the approach proposed in Lutz et al. (2019) is consecutively briefly recalled and summarized. The cost function's time derivative is given by

$$\frac{\mathrm{d}J(\boldsymbol{u})}{\mathrm{d}t} = \left(\frac{\mathrm{d}\boldsymbol{u}}{\mathrm{d}t}\right)^{\mathrm{T}} \nabla_{\boldsymbol{u}} J(\boldsymbol{u}) = [\dot{u}_1 \cdots \dot{u}_m] \begin{bmatrix} \frac{\partial}{\partial u_1} J(\boldsymbol{u}) \\ \vdots \\ \frac{\partial}{\partial u_m} J(\boldsymbol{u}) \end{bmatrix} \quad (1)$$

with $\nabla_{\boldsymbol{u}} J(\boldsymbol{u})$ denoting the gradient of the cost function with respect to the input vector. The UKF estimator states $\boldsymbol{x}(t) \in \mathbb{R}^n$ are chosen as the vector of partial derivatives of the cost function with respect to the $m = n-1$ components of the input vector appended by the cost function, thus

$$\boldsymbol{x} = \begin{bmatrix} \frac{\partial}{\partial u_1} J(\boldsymbol{u}) \\ \vdots \\ \frac{\partial}{\partial u_m} J(\boldsymbol{u}) \\ J(\boldsymbol{u}) \end{bmatrix} = \begin{bmatrix} x_1 \\ \vdots \\ x_{n-1} \\ x_n \end{bmatrix}. \quad (2)$$

Since in general the time variant system $\Sigma(t, \boldsymbol{u})$ is unknown apriori the time derivative of the gradient is modeled to be zero with additive white process noise $\hat{\boldsymbol{w}} = [w_1, \ldots, w_m]^{\mathrm{T}}$ with covariance $Q \in \mathbb{R}_+^{m \times m}$. Therewith the estimator state differential equation follows as

$$\dot{\boldsymbol{x}} = \begin{bmatrix} 0 \\ \vdots \\ 0 \\ \dot{\boldsymbol{u}}^{\mathrm{T}} H \boldsymbol{x} \end{bmatrix} + \begin{bmatrix} w_1 \\ \vdots \\ w_m \\ 0 \end{bmatrix}, \quad t > t_0, \; \boldsymbol{x}(t_0) = \boldsymbol{x}_0 \quad (3)$$

with $H = [I_m, \mathbf{0}_m] \in \mathbb{R}^{m \times n}$, where $I_m \in \mathbb{R}^{m \times m}$ is the identity matrix and $\mathbf{0}_m$ is the zero vector. Integrating (1)-(3) into the ESC algorithm according to Fig. 1 yields the time derivative of the system input

$$\dot{\boldsymbol{u}} = \boldsymbol{d} + \boldsymbol{k}(\nabla_{\boldsymbol{u}} J)_{\text{est}} = \boldsymbol{d} + \boldsymbol{k}(H\boldsymbol{x}), \quad (4)$$

where $\boldsymbol{d}(t) \in \mathbb{R}^m$ is the perturbation signal and $\dot{\boldsymbol{u}}(t) \in \mathbb{R}^m$. Different to Lutz et al. (2019) the gain $\boldsymbol{k}$ is a vector and

not scalar to be able to weight the degrees of freedom independently. The full process model of the gradient estimator with $\boldsymbol{w} = [\hat{\boldsymbol{w}}^{\mathrm{T}}\ 0]^{\mathrm{T}}$ reads as

$$\begin{aligned}\dot{\boldsymbol{x}} &= \begin{bmatrix} 0 \\ \vdots \\ 0 \\ \boldsymbol{d}^{\mathrm{T}} H \boldsymbol{x} + \boldsymbol{k}^{\mathrm{T}} (\boldsymbol{x}^{\mathrm{T}} H^{\mathrm{T}}) H \boldsymbol{x} \end{bmatrix} + \boldsymbol{w} \\ &= \boldsymbol{f}(\boldsymbol{x}, \boldsymbol{d}) + \boldsymbol{w}, \quad t > t_0, \quad \boldsymbol{x}(t_0) = \boldsymbol{x}_0 \end{aligned} \tag{5a}$$

with the measurement equation

$$y = J(\boldsymbol{u}) + l, \tag{5b}$$

where l is white measurement noise with covariance $R > 0$. The output equation of the filter is choosen as

$$\hat{y} = \hat{x}_n + l = h(\hat{\boldsymbol{x}}) + l. \tag{5c}$$

To obtain $\boldsymbol{x}$ defined in (3) from the measurement (5b) a nonlinear filter is set up and integrated into the approach. Here, the UKF is used since it is easier to implement and the nonlinearities are captured more accurately (Julier and Uhlmann, 2004).

2.2 Constrained Extremum-seeking control

To prevent the system from leaving its feasible operation area or to react to input constraints a penalty function can be introduced as shown in Fig. 1. Such constraints are formulated according to

$$h_l(\boldsymbol{u}, \boldsymbol{y}) \geq 0, \qquad l \in 1, ..., k \tag{6}$$

where k is the number of constraints. As pointed out by Lutz et al. (2019) and Guay et al. (2015) the use of a penalty function over a strict barrier function is favorable in ESC, where the system might temporarily be pushed out of the feasible operation area. The penalty function considered in this paper was proposed by Lutz et al. (2019) and is of the form

$$p_1(x) = \begin{cases} \mu \ln(x), & \text{for } x > \epsilon \\ \mu\, q(x), & \text{else} \end{cases}, \tag{7}$$

where $q(x)$ denotes the truncated Taylor series expansion of the logarithm in x

$$q(x) = q_0 + q_1 x + q_2 x^2 \tag{8}$$

at $\epsilon > 0$ with $q_0 = \ln \epsilon$, $q_1 = \epsilon^{-1}$ and $q_2 = -\epsilon^{-2}$. The penalty function $p(\boldsymbol{u}, \boldsymbol{y})$ as shown in Fig. 1 is defined as $p(\boldsymbol{u}, \boldsymbol{y}) = \Sigma_{l=1}^{k} p_1(h_l(\boldsymbol{u}, \boldsymbol{y}))$.

2.3 Integration of the UKF based ESC into a behavioral approach

In the case of plume tracking the turbidity and / or the redox potential of the water can be used as the cost function that is to be maximized. Since the turbidity can be sensed the furthest away from the vent it is chosen in this paper. The system $\Sigma(t, \boldsymbol{u})$ denotes the AUV dynamics within a water body. Thus the system input $\boldsymbol{u}$ is defined as the desired position and orientation of the water property sensor of the AUV, which are assumed to be realized by a suitable controller, and the system output $\boldsymbol{y}$ is the vector of the measured water properties. The turbidity sensor works via optical backscattering. The boundary between the ambient water and the plume is sharp so that the influence of the orientation of the sensor on the measured turbidity can be neglected. Therefore the system input is chosen as the position vector $\boldsymbol{u} = [x, y, z]^{\mathrm{T}}$. In the described plume scenario the penalty function can be used to restrict the search to the average depth z_{av} in which the plume was measured so far and to greater depth. This translates to the input constraint $h_1(\boldsymbol{u}) = z - z_{\mathrm{av}} + z_{\mathrm{tol}} \geq 0$, where z_{tol} is the tolerance depth, which has to be chosen based on the perturbation amplitude in z-direction and the expected plume dimensions. The time average of the plume follows a Gaussian distribution. Hence on the center line of the plume the turbidity is the highest and increases with decreasing distance to the vent. However, the turbidity gradient along the center line of the plume is very small so that pure extremum seeking would be too slow, therefore the ESC is combined with a behavioral approach that exploits domain knowledge. The possible behaviors are *search plume, drive up-current, re-enter plume* and *3D ESC*. The switching between the behaviors is shown in the state machine in Fig. 2. Here S_{p} is the state or behavior with the consecutively numbered index p that is increased at every state transition.

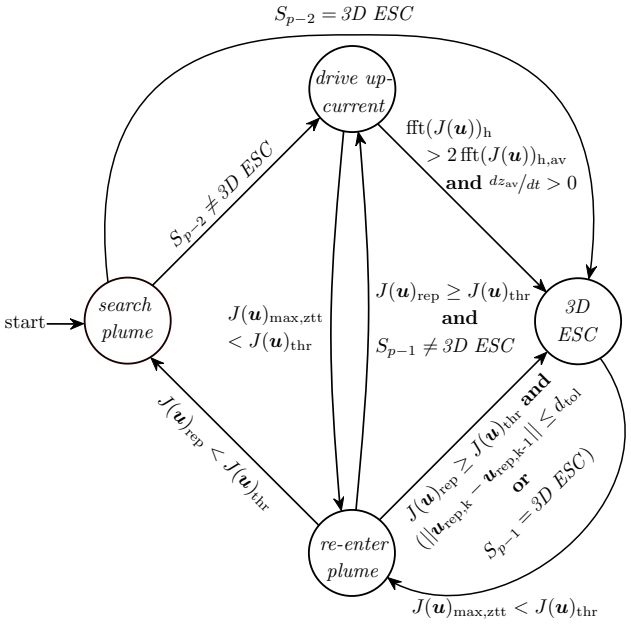

Fig. 2. State machine describing the transitions between the four search behaviors.

Start: At the start of the search procedure the current flow direction is estimated or measured. In case the AUV is equipped with an ADCP this should be used, otherwise the AUV can be commanded to only control its depth and let itself drift with the current for a short amount of time. Based on the start and end position of the drift the current direction can be approximated. This is sufficient since obtaining the exact spatial and temporal distribution of the plume is infeasible which would be needed to always drive in the right direction to follow the horizontal plume bending. After the measurement or estimation of the current direction the state transitions to the *search plume* behavior.

Search plume: In the *search plume* behavior the AUV drives a zigzag trajectory across the current direction in the depth corresponding to the maximum cost function measured so far. At the start this depth is chosen based

on precedent ship based measurements that are done to determine the search area for the AUV. Alternatively the AUV can drive a Yoyo pattern in z-direction until contact with the plume is achieved. The first time the horizontal crossing of the plume is performed slightly up-current and all other times slightly down-current. The latter is beneficial in case the AUV overshoots the plume source. While crossing the plume its center is estimated by averaging the positions where the AUV enters and leaves the plume. The behavior ends with driving to the estimated plume center in cross current direction and transitions to the state *drive up-current* if $S_{p-2} \neq$ *3D ESC* and else to *3D ESC*.

Drive up-current: In the *drive up-current* behavior the ESC is used for the vertical and the cross current axis to keep the AUV within the plume. Simultaneously it is commanded to drive in the direction opposite to the current with the up-current velocity v_{uc} to make progress towards the source. A major difference compared to the approaches in Li et al. (2006); Tian et al. (2014, 2015); Wang et al. (2020) is that the AUV depth is not constant in this case but the ESC is used to also detect gradients in z-direction, which, e.g., occur when the plume is bending towards its source. Two state transitions are possible in this behavior. First, if the AUV fails to measure a significant turbidity value for the duration of the zero turbidity timeout t_{ztt} the state transitions to the *re-enter plume* behavior. This translates to $J(\boldsymbol{u})_{\mathrm{max,ztt}} < J(\boldsymbol{u})_{\mathrm{thr}}$, where $J(\boldsymbol{u})_{\mathrm{max,ztt}}$ is the maximum of the cost function within the last t_{ztt} and $J(\boldsymbol{u})_{\mathrm{thr}}$ is a tunable threshold. The zero turbidity timeout should be chosen based on the cross plume perturbation signal frequency and the forward velocity of the AUV. Second, if it is likely that the AUV is at the position, where the plume is bending towards its source the state will transition to the *3D ESC* behavior. This is the case if $\mathrm{fft}(J(\boldsymbol{u}))_{\mathrm{h}} > 2\,\mathrm{fft}(J(\boldsymbol{u}))_{\mathrm{h,av}}$ and ${}^{dz_{\mathrm{av}}}\!/_{dt} > 0$. Here $\mathrm{fft}(\cdot)$ is the fast Fourier transform, the index h refers to the high frequency components and the index av to a moving average value. This condition is motivated by the fact that the plume diameter is decreasing with decreasing distance to the plume source. Hence the turbidity gradient across the current direction is stronger in the vicinity of the source, especially when the AUV leaves the plume and re-enters which happens more often in this area compared to the search in the wide plume far away from the source.

Re-enter plume: In the *re-enter plume* behavior the AUV drives to the position corresponding to the maximum cost function measured in the last t_{ztt}. Here, three state transitions are possible. First, if the cost function at the re-enter position $J(\boldsymbol{u})_{\mathrm{rep}}$ is smaller than the threshold $J(\boldsymbol{u})_{\mathrm{thr}}$ the state transitions to the *search plume* behavior. Second, if $J(\boldsymbol{u})_{\mathrm{rep}} \geq J(\boldsymbol{u})_{\mathrm{thr}}$ and $S_{p-1} \neq$ *3D ESC* the state transitions to the *drive up-current* behavior. Third, if $J(\boldsymbol{u})_{\mathrm{rep}} \geq J(\boldsymbol{u})_{\mathrm{thr}}$ and either $S_{p-1} =$ *3D ESC* or the current and the last re-enter plume position are at maximum the tolerance distance d_{tol} apart from each other, hence $||\boldsymbol{u}_{\mathrm{rep,k}} - \boldsymbol{u}_{\mathrm{rep,k\text{-}1}}|| \leq d_{\mathrm{tol}}$ the state transitions to the *3D ESC* behavior. Here $\boldsymbol{u}_{\mathrm{rep,k}}$ is the position where the AUV re-enters the plume the k-th time the *re-enter plume* behavior is performed and $||\cdot||$ denotes the euclidean norm.

3D ESC: In the *3D ESC* behavior the ESC is used for all three degrees of freedom x, y and z. Additionally the small positive constants $v_{x,\mathrm{3D}}$ and $v_{z,\mathrm{3D}}$ are added to the perturbation signal in x- and z-direction respectively to accelerate the search for the plume source. The source is declared to be found when the AUV reaches the depth that corresponds to half the plume height and is still measuring a significant turbidity. Afterwards fine grained measurements can be done as e.g. photo surveys in the classical Lawnmover patterns.

3. SIMULATION FRAMEWORK

3.1 AUV dynamics

The AUV considered in this paper is the Girona500 AUV from iquarobotics (iquarobotics, 2016). It is rated for up to 500 m depth and therefore only suitable for shallow vents like, e.g., in lakes such as the Yellowstone lake (Sohn et al., 2019) or shallow vent sites in the sea such as listed in Zhang et al. (2020). The AUV is equipped with five thrusters in an underactuated configuration such that the roll movement can not be controlled but by construction the roll motion is stable. It is a hoovering AUV with high maneuverability and able to make sharp turns, therefore *Assumption 2* in Sec. 2.1 is valid as long as the ESC parameters are chosen appropriately. For large torpedo shaped AUVs with limited maneuverability this assumption is not valid, especially in the *3D ESC* state. Therefore measures would have to be taken, e.g. pausing the UKF based ESC in phases where the AUV is not able to track the desired trajectory and planning a new trajectory to bring the AUV back on track. The mathematical model of the AUV considered in this paper reads

$$\dot{\boldsymbol{\eta}} = R_{\boldsymbol{\Theta}}(\boldsymbol{\eta})\boldsymbol{\nu} \tag{9a}$$

$$M\dot{\boldsymbol{\nu}} = -C(\boldsymbol{\nu})\boldsymbol{\nu} - D(\boldsymbol{\nu})\boldsymbol{\nu} + B\boldsymbol{\tau}. \tag{9b}$$

Here $\boldsymbol{\eta} = [x, y, z, \phi, \theta, \psi]^{\mathrm{T}}$ defines the earth fixed position vector with x, y, z given in the North-East-Down (NED) frame and the roll, pitch and yaw angles, respectively. The input matrix $B \in \mathbb{R}^{6\times5}$ is composed of zero elements only except for $B_{1,1} = B_{2,2} = B_{3,3} = B_{5,4} = B_{6,5} = 1$ (Fossen, 2011). The body fixed velocity vector $\boldsymbol{\nu} = [u, v, w, p, q, r]^{\mathrm{T}}$ contains the surge, sway, heave, roll, pitch, and yaw and $\boldsymbol{\tau} = [\tau_u, \tau_v, \tau_w, \tau_q, \tau_r]^{\mathrm{T}}$ is the control vector with the respective forces τ_u, τ_v, τ_w and moments τ_q, τ_r. The transformation from body fixed into earth fixed coordinates is described in (9a) via the rotation matrix $R_{\boldsymbol{\Theta}}(\boldsymbol{\eta})$ while (9b) describes the motion of the ship in body fixed coordinates with the inertia matrix M, Coriolis matrix C and damping matrix D. For the Girona500 AUV accurate modeling parameters are not available, therefore M and D are implemented as diagonal matrices with estimated parameters based on the specifications by iquarobotics. The underlying motion control system is chosen as a PID controller.

3.2 Simulation environment and data

The simulations are performed in a framework build upon the Robot Operating System (ROS), the robot simulator Gazebo and the Unmanned Underwater Vehicle (UUV)

simulator introduced in Manhes et al. (2016). Gazebo produces realistic robot motions for land based robots due to its built in physics engines. The UUV simulator provides custom plugins that integrate the hydrodynamic forces and moments in the Gazebo physics engine. ROS can be seen as the middleware for the other two and is e.g. used for coordinate transformations and message-passing.

As simulation data the chemical plume from Manhães et al. (2019) is used which is a complementary GIT repository to the UUV simulator and is an implementation of the plume model presented in Tian and Zhang (2010). The dynamic fluid flow and the particle plume are treated independent from each other meaning that the buoyant plume does not affect the fluid flow. For the latter the build in current simulation of Gazebo is used. The plume is treated as a passive scalar turbulence and the Lagrangian particle random walk approach is used to solve the plumes' differential equations. The shape of the plume can be parameterized by the turbulent diffusion coefficients in x, y and z, the buoyancy flux and stability parameter of the particles that together define the plume rise height. Furthermore the number of particles that are emitted from the source per iteration can be set, which defines how dense the plume will be. To make the simulation computationally more efficient, the maximum number of particles can be defined as well as an operation area. If a particle drifts out of this area it is deleted.

4. SIMULATION RESULTS

The simulated plume has its origin at $[0, 0, 40]^{\mathrm{T}}$ m and has a height of ≈ 20 m. The operation area is set to the ranges $x \in (-20\,\mathrm{m}, 350\,\mathrm{m})$ and $y \in (-60\,\mathrm{m}, 60\,\mathrm{m})$ for both, the AUV and plume particles. Figure 3 shows the plume as a point cloud for the time steps $t = 0$ min in subplot a), $t = 15$ min in b) and $t = 30$ min in c) overlaid by the AUV path. The depth of the AUV and plume particles is color coded. To make the plume simulation as realistic as possible the water currents are not static but subject to significant changes in terms of velocity and vertical and horizontal angles during the simulation period. As a result the plume height is also slightly varying in the non-buoyant phase. The AUV start position is given as $[300, -60, 20]^{\mathrm{T}}$ m. In Fig. 4 the turbidity and penalty function are shown over time in subplot a) together with the desired and actual AUV path in x, y and z in subplots b), c) and d) respectively. The different behaviors can be seen in the last three subplots as well as in Fig. 3. Switching of the states is marked by the stars in Fig. 3 and horizontal dashed lines in Fig. 4. At first the drift maneuver described in Sec. 2.3 is performed, where the AUV drifts mainly in positive x-direction. It is followed by the *search plume* behavior in which the AUV drives mainly in y-direction while searching the plume and estimating its center which is found at $t = 5$ min. After the AUV has reached the plume center the *drive up-current* behavior is performed until $t \approx 28$ min, where the AUV leaves the plume and subsequently performs the *re-enter plume* behavior. After four iterations of *drive up-current* and *re-enter plume* the last two *re-enter plume* positions are close to each other so that the *3D ESC* behavior is performed. Within two minutes the AUV follows the plume to half its height, where the exit condition is fulfilled. Considering

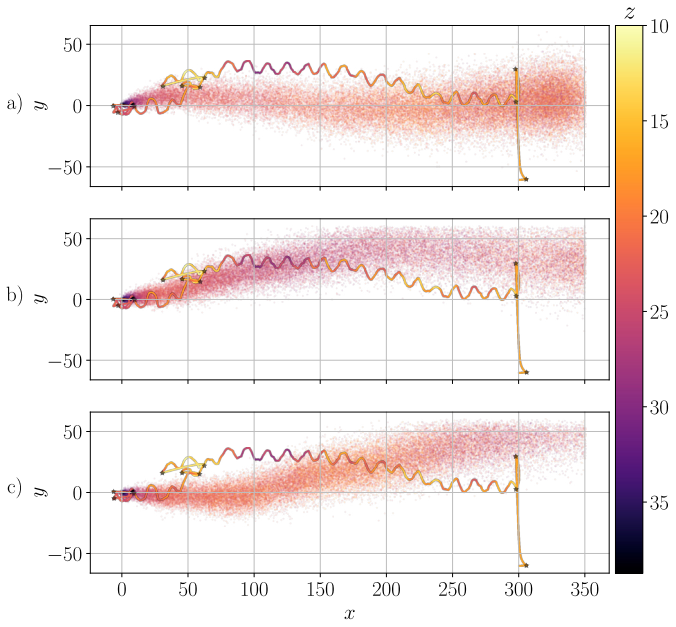

Fig. 3. Scatter plot of the plume particles for a) $t = 0$ min, b) $t = 15$ min and c) $t = 30$ min and AUV path in the x-y-plane and color coded depth for both, plume particles and AUV path. Stars indicate state switching.

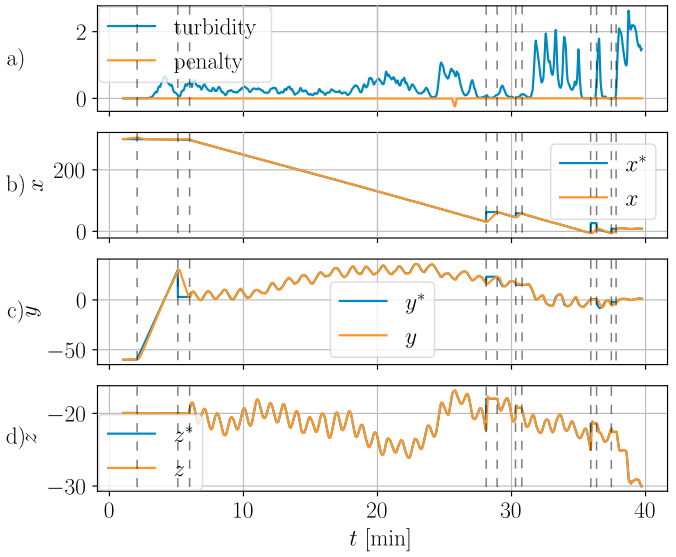

Fig. 4. Turbidity and penalty function over time in subplot a) and desired and actual AUV path in x, y and z in subplots b), c) and d) respectively. The horizontal dashed lines indicate state switching.

Fig. 3 b) and Fig. 4 d) at ≈ 20 min one can see that the method is able to not only follow the plume in the x-y-plane but also in z-direction. The penalty function in Fig. 4 a) is almost zero except for $t \approx 26$ min, where the AUV shortly exceeds the z_{tol} until the ESC increases the depth to within the tolerance depth. The AUV oscillates in y- and z-direction which is desired as long as the plume source is not found because the ESC needs significant changes in these directions to estimate the gradient of the cost function w.r.t. the AUV position. Parameters used in the simulation are given in Tab. 1. The ESC parameters are

Table 1. ESC and plume parameters used in simulations. Vectors represent the parameters in x, y and z.

Period perturbation signal $\boldsymbol{T}_\mathrm{p}$	$[83, 71, 59]^\mathrm{T}$ s
Amplitude perturbation signal $\boldsymbol{A}_\mathrm{p}$	$[0.008, 0.020, 0.008]^\mathrm{T}$ m
Signal shape perturbation signal	cosine
Optimization gain $\boldsymbol{k}$	$[1.5, 6.0, 1.5]^\mathrm{T} \cdot 10^{-3}$
Covariance Q	$\mathrm{diag}(5 \cdot 10^{-4}, 5 \cdot 10^{-4}, 5 \cdot 10^{-3})$
Covariance R	$5 \cdot 10^{-3}$
Parameter UKF α	1
Parameters UKF β, γ	0
Up-current velocity v_uc	$0.2 \frac{\mathrm{m}}{\mathrm{s}}$
Perturbation signal offset $v_{x,\mathrm{3D}}$	$0.05 \frac{\mathrm{m}}{\mathrm{s}}$
Perturbation signal offset $v_{z,\mathrm{3D}}$	$0.05 \frac{\mathrm{m}}{\mathrm{s}}$
Tolerance depth z_tol	4 m
Penalty function, μ	$1 \cdot 10^{-3}$
Penalty function, ϵ	$5 \cdot 10^{-2}$
Zero turbidity timeout t_ztt	41.5 s
Re-enter plume time t_rep	120 s
Cost function threshold $J(\boldsymbol{u})_\mathrm{thr}$	0.1
Re-enter tolerance distance d_tol	5 m
Plume simulation parameters	
Turbulent diffusion coefficients	$[0.035, 0.035, 0.035]^\mathrm{T}$
Buoyancy flux	0.08
Stability parameter	0.001
Particles per iteration	50

chosen based on the AUV and sensor dynamics so that input constraints do not need to be considered. However if they shall be addressed this can be done via penalty functions as described in Lutz et al. (2019).

5. CONCLUSION

An UKF based ESC approach is combined with domain knowledge to address chemical plume tracking using an AUV. For this a behavioral approach with ESC as the base mode is constructed as a state machine. In contrast to existing approaches in the literature the proposed method is able to simultaneously make progress towards the plume source and to follow the plume in the vertical direction. The effectiveness is demonstrated by a simulation of a 3D plume and a 6 DoF AUV model.

Future research will include water tests with either an artificial plume of Rhodamine dye or in a shallow vent field. Furthermore the simulation will be extended to larger and faster AUVs to validate that the method can also be applied to large kilometer size deep sea plumes.

REFERENCES

Baker, E. T., 2014. Hydrothermal Plumes. Encyclopedia of Marine Geosciences (1995), 1–7.

Elkinton, J. S., Hal, C., Onot, T., Carde, R. T., 1987. Pheromone puff trajectory and upwind flight of male gypsy moths in a forest. Physiological Entomology 12 (4), 399–406.

Ferri, G., Jakuba, M. V., Yoerger, D. R., 2010. A novel trigger-based method for hydrothermal vents prospecting using an autonomous underwater robot. Autonomous Robots 29 (1), 67–83.

Fossen, T. I., 2011. Handbook of Marine Craft Hydrodynamics and Motion Control. John Wiley & Sons.

Guay, M., Moshksar, E., Dochain, D., 2015. A constrained extremum-seeking control approach. International Journal of Robust and Nonlinear Control 25 (16), 3132–3153.

Hu, H., Song, S., Chen, C. L., 2019. Plume Tracing via Model-Free Reinforcement Learning Method. IEEE Transactions on Neural Networks and Learning Systems 30 (8), 2515–2527.

iquarobotics, 2016. Girona500 auv. URL `https://iquarobotics.com/girona-500-auv`

Jakuba, M. V., Yoerger, D. R., 2008. Autonomous search for hydrothermal vent fields with occupancy grid maps. Proceedings of the 2008 Australasian Conference on Robotics and Automation, ACRA 2008.

Julier, S. J., Uhlmann, J. K., 2004. Unscented filtering and nonlinear estimation. Proceedings of the IEEE 92 (3), 401–422.

Li, W., Farrell, J. A., Pang, S., Arrieta, R. M., 2006. Moth-inspired chemical plume tracing on an autonomous underwater vehicle. IEEE Transactions on Robotics 22 (2), 292–307.

Lutz, M., Freudenthaler, G., Roduner, C., Meurer, T., 2019. Ukf-based constrained extremum-seeking control with application to a large-bore gas engine. In: 2019 IEEE 58th Conference on Decision and Control (CDC). pp. 561–566.

Manhães, M. M. M., Scherer, S. A., Voss, M., Douat, L. R., Rauschenbach, T., 2019. UUV plume simulator. URL `https://github.com/uuvsimulator/uuv_plume_simulator`

Manhes, M. M. M., Scherer, S. A., Voss, M., Douat, L. R., Rauschenbach, T., 2016. UUV simulator: A gazebo-based package for underwater intervention and multi-robot simulation. In: OCEANS 2016 MTS/IEEE Monterey. pp. 1–8.

Sohn, R. A., Luttrell, K., Shroyer, E., Stranne, C., Harris, R. N., Favorito, J. E., 2019. Observations and Modeling of a Hydrothermal Plume in Yellowstone Lake. Geophysical Research Letters 46 (12), 6435–6442.

Tian, Y., Li, W., Zhang, F., 2015. Moth-inspired plume tracing via autonomous underwaer vehicle with only a pair of separated chemical sensors. In: OCEANS 2015-MTS/IEEE Washington. IEEE, pp. 1–8.

Tian, Y., Zhang, A., 2010. Simulation environment and guidance system for AUV tracing chemical plume in 3-dimensions. CAR 2010 - 2010 2nd International Asia Conference on Informatics in Control, Automation and Robotics 1, 407–411.

Tian, Y., Zhang, A., Li, W., Yu, J., Li, Y., Zeng, J., 2014. A behavior-based planning strategy for deep-sea hydrothermal plume tracing with autonomous underwater vehicles. Oceans 2014 - Taipei, 1–10.

Vergassola, M., Villermaux, E., Shraiman, B. I., 2007. 'Infotaxis' as a strategy for searching without gradients. Nature 445 (7126), 406–409.

von See, T. B., Meurer, T., Greinert, J., 2021. Marine boundary layer tracking using an auv with ukf based extremum seeking. IFAC-PapersOnLine 54 (16), 320–326.

Wang, L., Pang, S., Xu, G., 2020. 3-dimensional hydrothermal vent localization based on chemical plume tracing. In: Global Oceans 2020: Singapore–US Gulf Coast. IEEE, pp. 1–7.

Zhang, Z., Fan, W., Bao, W., Chen, C.-T. A., Liu, S., Cai, Y., 2020. Recent developments of exploration and detection of shallow-water hydrothermal systems. Sustainability 12 (21), 9109.